Identifying FeLoBAL quasars in SDSS DR7Q with the convolutional neural network

He, Z.-Q.; Fu, Y.-M.; Wu, X.-B.; He, L.-X.

Citation
He, Z. -Q., Fu, Y. -M., Wu, X. -B., & He, L. -X. (2025). Identifying FeLoBAL quasars in SDSS DR7Q with the convolutional neural network. *Chinese Astronomy And Astrophysics*, *49*(4), 756-772. doi:10.1016/j.chinastron.2025.11.005

Version:	Publisher's Version
License:	Leiden University Non-exclusive license
Downloaded from:	https://hdl.handle.net/1887/4288608

Note: To cite this publication please use the final published version (if applicable).

ELSEVIER

CrossMark

CHINESE
ASTRONOMY
AND ASTROPHYSICS

Chinese Astronomy and Astrophysics 49-4 (2025) 756–772

Identifying FeLoBAL Quasars in SDSS DR7Q with the Convolutional Neural Network† ⋆

HE Zi-qi[1,2△] FU Yu-ming[3,4] WU Xue-bing[1,2△△] HE Ling-xue[5]

[1] *Department of Astronomy, School of Physics, Peking University, Beijing 100871*

[2] *Kavli Institute for Astronomy and Astrophysics, Peking University, Beijing 100871*

[3] *Leiden Observatory, Leiden University, Leiden NL-2300 RA*

[4] *Kapteyn Astronomical Institute, University of Groningen, Groningen NL-9700 AV*

[5] *Graduate School of Engineering, The University of Tokyo, Tokyo 1138656*

Abstract The Fe Low-ionization Broad Absorption Line Quasar (FeLoBALQ) is one of the rarest types of all quasars. Quasars blow out the surrounding violently, forming extreme outflows from which low ionized elements e.g. Fe provide the absorbing feature in FeLoBALQ spectra. Carrying high kinetic energy, the outflows of FeLoBALQ may possibly be enough for powering the $M - \sigma_*$ relationship between the supermassive black hole mass M and the host-galaxy bulge velocity dispersion σ_*. On the other hand, evidence has been found for the coexistence of FeLoBALQ with hosts' starburst or recent major merger. However, the FeLoBALQ sample collected so far is not large enough to stand for these theories statistically. This research focuses on digging out hidden FeLoBALQs from large quasar surveys, forming a FeLoBALQ catalog large enough for statistical and physical analyze. Adopting Convolutional Neural Network (CNN) method, 160 FeLoBALQs are newly identified from totally 50931 quasars in the SDSS (Sloan Digital Sky Survey) DR7Q (Data Release 7 Quasar catalog) in the redshift range of $0.8 < z < 2.125$, with previous identified FeLoBALQ spectra as training sample. The FeLoBALQs' color is found redder than normal quasars, and previously identified FeLoBALQs are lightly redder than newly identified ones; these differences are more obvious on bluer end than on redder end, and nearly disappear in mid-infrared band. The proportion of FeLoBALQs out of all quasars given is 0.43%, higher than previous prediction, but may still be underestimated. Further researches may expand this method to larger samples e.g. SDSS DR16Q (Data Release 16 Quasar catalog) for larger FeLoBALQ sample,

† Supported by the National Natural Science Foundation of China (Grant Nos. 11927804 & 12133001)

Received 2024-05-15; revised version 2024-08-05

⋆ A translation of *Acta Astron. Sin.* Vol. 66, No. 3, 33.1–33.14, 2025

△ zqhe@pku.edu.cn

△△ wuxb@pku.edu.cn

0275-1062/01/$-see front matter © 2025 Elsevier Science B. V. All rights reserved.

PII:
10.1016/j.chinastron.2025.11.005

which may help to answer the questions of the relationship between FeLoBALQ and host galaxy star formation, FeLoBALQ and galaxy major merger, and the coevolution of galaxies and central supermassive black holes.

Key words galaxies: active, quasars: absorption lines, methods: deep learning, catalogs

1. INTRODUCTION

In Broad Absorption Line (BAL) quasars, Fe Low-ionization Broad Absorption Line Quasars (FeLoBAL Quasars, FeLoBALQs) represent an extremely peculiar subtype. The primary observational features of this type of quasars are characterized by Fe low-ionization absorption lines, predominantly FeII with occasional detections of FeIII, and are sometimes accompanied by strong absorption features from HeI, SiII, and NiII. Compared to the CIV absorption, which signifies High-ionization BALs (HiBALs), and the MgII absorption, which signifies Low-ionization BALs (LoBALs), the production of FeII absorption requires a lower temperature for its first ionization; this implies that the gaseous outflows in FeLoBALQs are located at a greater distance from the central core region compared to typical LoBAL quasars, suggesting that the gaseous outflow process in FeLoBALQs is more intense. Research indicates that establishing the well-known $M-\sigma_*$ relationship between supermassive black hole mass M and the host galaxy's bulge velocity dispersion σ_* during the co-evolution of galaxies and their central black holes requires approximately 5% of the quasar's bolometric luminosity[1, 2]. Moreover, research by Moe et al.[3] indicates that the kinetic luminosity of the outflows in FeLoBALQs reaches 1% of the bolometric luminosity, constituting a significant component of the driving energy for the co-evolution. Research by Faucher-Giguère et al.[4] furthermore indicates that for the most luminous FeLoBALQs, the kinetic luminosity constitutes approximately 2%–5% of the bolometric luminosity — a fraction even sufficient to entirely drive the co-evolution. This body of research demonstrates that FeLoBALQs likely play a significant role in establishing the co-evolutionary relationship between central black holes and their host galaxies.

Since the discovery of FeLoBALQs, the physical mechanisms and origins underlying this type of quasars have remained pressing questions awaiting resolution. However, limited by the scarcity of such objects, progress in relevant research has consistently been non-systematic, making it difficult to produce statistically convincing findings. Firstly, regarding the formation mechanisms of FeLoBALQs, research has failed to reach a consensus. Research by Yuan et al.[5] and Runnoe et al.[6] reveals that BAL quasars exhibit weaker [OIII] but stronger FeII emission lines, implying higher accretion rates compared to non-BAL quasars. However, research by Schulze et al.[7] on LoBAL quasars and FeLoBALQs, as well as research by Rankine et al.[8] on BAL quasars, suggest that the accretion rates of BAL quasars and its subtypes such as LoBAL quasars and FeLoBALQs are consistent with those of non-BAL quasars, which contradicts previous findings.

Moreover, research has not established a unified model for the origins of FeLoBALQs. In 2010, Farrah et al.[9] proposed that FeLoBALQs may exist in environments that satisfy the following three conditions: (1) The galaxy is in the final stage of a major merger-driven starburst; (2) The luminous quasar is in the late phase of accreting the surrounding dust; (3) The system is viewed from a specific observing angle. The aforementioned origins have found support in some research. Research of Ultraluminous Infrared Galaxies (ULIRGs) by Farrah et al.[10] in 2005 led to the discovery of four ULIRGs with quasars at their cores, one of which was identified as a FeLoBALQ. The extreme infrared luminosity of ULIRGs indicates a high abundance of warm gas and dust as well as an extremely high star formation rate. Infrared observations of nine FeLoBALQs by Farrah et al.[11] in 2007 demonstrated the consistency of their infrared luminosities with those of ULIRGs, with their optical features signaling star formation rates at hundreds of solar masses per year; the research posits that there must be a certain connection between FeLoBALQs and the extremely high star formation rates in ULIRG host galaxies, suggesting a likely co-evolutionary process between quasars and their host galaxies. The high-resolution observations conducted by Lawther et al.[12] on FeLoBALQs confirmed the occurrence of major mergers in their environments. However, some research has challenged the aforementioned origins. The submillimeter observations of 17 FeLoBALQs conducted by Violino et al.[13] did not confirm the connection between FeLoBALQs and the star formation activity in their host galaxies. High-resolution observations by Villforth et al.[14] found no evidence of major mergers in the environments of FeLoBALQs.

The primary reason for the lack of a consistent conclusion in the aforementioned research is the limited sample size of currently identified FeLoBALQs, which makes investigations of such a small sample prone to significant contingency. Research on FeLoBALQs require a larger sample size to yield statistically convincing conclusions. The body of research on the spectral properties of FeLoBALQs by the team led by Leighly and Choi et al.[15–18], which utilized a sample of 50 FeLoBALQs, has represented the largest and most systematic investigation of such objects to date, with the findings exhibiting a high degree of consistency. Utilizing the spectral absorption features of FeLoBALQs to investigate outflows, the team discovered a positive correlation between outflow strength and velocity and the presence of outflow strengths sufficient to drive quasar feedback on the host galaxies in 18% of the FeLoBALQs[15]. The team investigated the emission line strengths in the FeLoBALQs, and found that the Hβ emission lines of FeLoBALQs are generally broader, implying either a relatively high inclination angle for observation of FeLoBALQs or an absence of gas emitting low-velocity spectral lines; based on the accretion rates calculated from emission line strengths, the FeLoBALQs were classified into two types: those with low luminosities and low accretion rates, and those with high luminosities and high accretion rates[16]. Using models, the team investigated the actual locations of broad absorption line features in the spectra of these two types of FeLoBALQs, and found that for the high-luminosity type, the distance

from the quasar center to the broad absorption line region is negatively correlated with the accretion rate, whereas a positive correlation for the low-luminosity type[17]. The team compared the Spectral Energy Distributions (SEDs) of FeLoBALQs with those of normal quasars, and found that FeLoBALQs exhibit significant differences in their emission lines and other parameters from both LoBAL and normal quasars, suggesting that FeLoBALQs may represent an extremely peculiar type of quasars[18].

Supported by a medium-sized sample of FeLoBALQs, the aforementioned body of research yielded findings with a considerable degree of generality. However, in order to verify the accuracy of the aforementioned theories and support more systematic research on the properties of FeLoBALQs, a larger sample of FeLoBALQs is essential. This research aims to perform a large-scale search for and identification of FeLoBALQs to effectively expand their sample size, thereby providing crucial data support for their systematic investigation, and establishing an essential statistical foundation for frontier research areas, including galaxy-AGN co-evolution, quasar structure and physical properties, as well as quasar classification and population statistics.

The research methodology of this paper involves employing a Convolutional Neural Network (CNN) from the field of machine learning[19]. By feeding spectra of FeLoBALQs and normal quasars as the training sample, the program acquires the capability to identify whether a spectrum belongs to a FeLoBALQ. This trained model is then applied to the existing Data Release 7 Quasar catalog (DR7Q) of the Sloan Digital Sky Survey (SDSS)[20] to identify previously unidentified FeLoBALQ spectra, thereby providing a robust sample foundation for future systematic research of FeLoBALQs. Due to the relatively low incidence of FeLoBALQs and the potential confusion of their FeLoBAL absorption features with those of other BAL quasars, we restricted the redshift range of both the training and target samples to $0.8 < z < 2.125$ to enhance the identification accuracy of the CNN and minimize the interference of other BAL quasars with FeLoBALQ identification, so that the rest-frame 2000–3200 Å absorption features of interest fall entirely within the effective spectral coverage.

Chapter 2 of this paper introduces the training and target samples, the CNN machine learning methodology, as well as the research process and key implementation details. Chapter 3 presents the results of FeLoBALQ identification and discusses potential improvements. Chapter 4 provides a comprehensive summary of the research, clarifies its scientific significance, and outlines prospects for future work.

2. SAMPLES AND METHODOLOGY

2.1 Redshift Selection and Target Sample

During the initial testing phase, we employed raw spectra for CNN training and identification. It was observed that a significant fraction of the spectra classified as FeLoBALQs were from BAL quasars exhibiting broad absorption solely from CIV or MgII, with no apparent

FeII absorption. Preliminary analysis revealed that the absorption profiles of different types of BALs are relatively similar; aside from the absorption troughs caused by continuous absorption in FeLoBALs, most exhibit Gaussian-like profiles. Furthermore, redshift effects allow absorption lines to appear at any wavelength across the entire spectrum, making it difficult for the program to determine whether an absorption line originates from FeII rather than other elements.

Therefore, we extracted the rest-frame 2000–3200 Å band from the spectra of both the training and target samples for our research, which encompasses the potential strong FeII absorption features and retains MgII as a reference, with no significant interference from other features such as CIV and AlIII. The primary contributors to the flux in this band are the quasar continuum, the FeII continuum emission, and the MgII broad emission line. Against this background, the FeII absorption features are well accentuated. Furthermore, absorption components other than MgII broad absorption lines cause minimal interference with the identification of FeLoBALs. Based on the 3600–10000 Å wavelength range of SDSS BOSS (Baryon Oscillation Spectroscopic Survey)/eBOSS (extended BOSS) spectra, we calculated and applied a redshift range of $0.8 < z < 2.125$ as a constraint to ensure that the quasar spectra, after redshift, essentially fully fall within this band, that is, their rest-frame 2000–3200 Å band is essentially completely covered by the SDSS BOSS/eBOSS spectra within this redshift range. In the SDSS DR7Q sample used in this research, the rest-frame wavelength at the red end for quasars at a redshift of approximately 2 may not reach 3200 Å, which nevertheless does not compromise the identification of FeLoBALQs. We therefore retained these quasars in our sample to facilitate future comparative research between the results from DR7Q and those from the Data Release 16 Quasar catalog (DR16Q)[21] after an extended investigation of FeLoBALQs based on DR16Q.

We selected the SDSS DR7Q catalog and, after applying the redshift constraint, obtained a total of 50931 spectra as the target sample. As a significant milestone of the SDSS, this sample has proven to be scientifically robust. Its moderate size facilitates the iteration of methodologies and the progression of research, while also allowing for straightforward extension of the research to the SDSS DR16Q sample.

Since many quasar spectra suffer from low signal-to-noise ratios, using the SDSS-provided ANDMASK or ORMASK to mask bad pixels in the spectra would result in the loss of a substantial amount of useful information. Therefore, we employed the sigma-clipping (σ-clipping) method to remove artifacts such as sky emission lines from the spectra. Subsequently, we converted the spectra to the rest frame, extracted the 2000–3200 Å band, and resampled them to one data point per angstrom to meet the requirement of the CNN program that all input data must have uniform length. We then subtracted the mean value of the spectral flux in this band from each data point to mitigate the continuum's influence on identification and accentuate absorption and emission features. Finally, we applied a smoothing process to the spectra before feeding them into the CNN to reduce noise in-

terference with identification and accentuate macroscopic features such as broad absorption lines.

2.2 Training Sample Selection

In order to train the CNN program, we compiled a sample of 220 FeLoBALQs from sources previously identified by other teams[22–35], and used the SDSS spectra of these FeLoBALQs to form the training sample. Among the 220 FeLoBALQ sources, 186 have counterparts in the SDSS database. By including multiple spectroscopic observations of the same source, we expanded the total number of FeLoBALQ spectra to 354. In order to ensure training quality, we retained only those spectra with high quality and evident FeII absorption lines, yielding a sample of 319 FeLoBALQ spectra. After applying the redshift constraint of $0.8 < z < 2.125$, the sample contained 167 FeLoBALQ spectra. During a trial run to validate the CNN's identification performance, we identified additional 33 FeLoBALQ spectra, which were also incorporated into the training sample to expand its size; finally, the training sample contained 200 FeLoBALQ spectra. We also incorporated 379 randomly selected non-FeLoBALQ spectra of varying quality into the training sample, thereby facilitating the program's identification of the unique features of FeLoBALQs. We employed the aforementioned 579 spectra as the total sample for the initial CNN training, which was randomly split into training and test sets at an approximate 3:1 ratio. The training set comprised 153 FeLoBALQ and 282 non-FeLoBALQ spectra for CNN training, while the test set contained 47 FeLoBALQ and 97 non-FeLoBALQ spectra to determine the iteration at which the CNN achieved stable identification accuracy. The CNN model that achieved stable accuracy at this iteration was then applied to the target sample for final identification. We applied the identical data processing procedure to the spectra in the training sample as we did to those in the target sample.

2.3 CNN Structure and Training

We chose to employ CNN for spectral identification primarily because of its renowned capability in image recognition, and a spectrum can be regarded as a one-dimensional image. We adopted a CNN structure of five alternating convolutional and pooling layers for spectral feature extraction; the five convolutional layers had core sizes of 3, 3, 5, 5, and 5, respectively, while the five pooling layers all had a core size of 2. We then fed the features into two fully connected layers comprising 360 and 50 hidden units, respectively, for the binary identification of FeLoBALQs. The Rectified Linear Unit (ReLU)[36, 37] was adopted as the activation function in the neural network to enhance robustness to noise and avoid vanishing gradients during training. A schematic diagram of the neural network structure is shown in Fig. 1.

The training sample was fed into the CNN, where the training set was used to train the model, and the test set was used to validate the training outcome and provide feedback to the model. The model's identification accuracy on the test set stabilized at 95% after 20 iterations; consequently, the model from this 20th iteration was selected and then applied

to the target sample for final identification, and its corresponding confusion matrix is shown in Fig. 2.

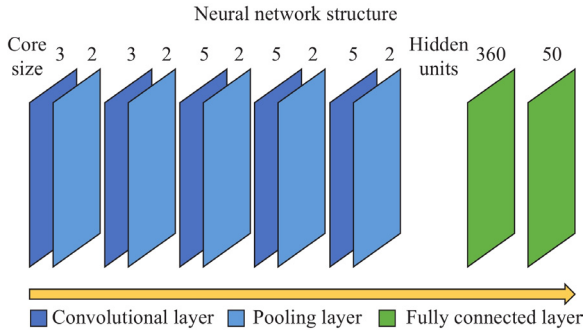

Fig. 1 Convolutional neural network structure of this research.

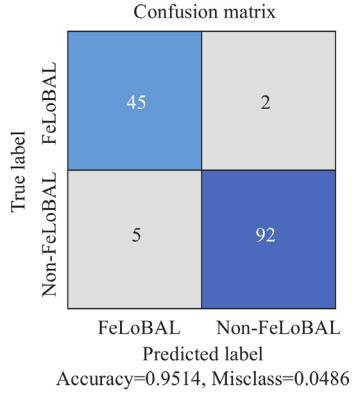

Fig. 2 Confusion matrix towards the test set when CNN stabilized at the 20th iteration.

3. RESULTS

We fed the aforementioned target sample into the trained CNN model, which identified approximately 1000 candidate spectra of FeLoBALQs. Through manual screening, we excluded spectra with weak or ambiguous FeII absorption features that precluded definitive identification, as well as those already present in the training sample. This process yielded a total of 160 newly identified FeLoBALQ spectra, including the 33 spectra identified during the trial run. A selection of these spectra is presented in Fig. 3. Appendix 1 presents the detailed information for the newly identified FeLoBALQs in this research, including SDSS Name, Right Ascension (RA) and Declination (Dec), SDSS spectroscopic identifiers (including Plate, Modified Julian Date [MJD], and Fiber), redshift (z), SDSS u, g, r, i, z band magnitudes (u, g, r, i, z), and WISE (Wide-field Infrared Survey Explorer) W1 and W2

band magnitudes (W1, W2).

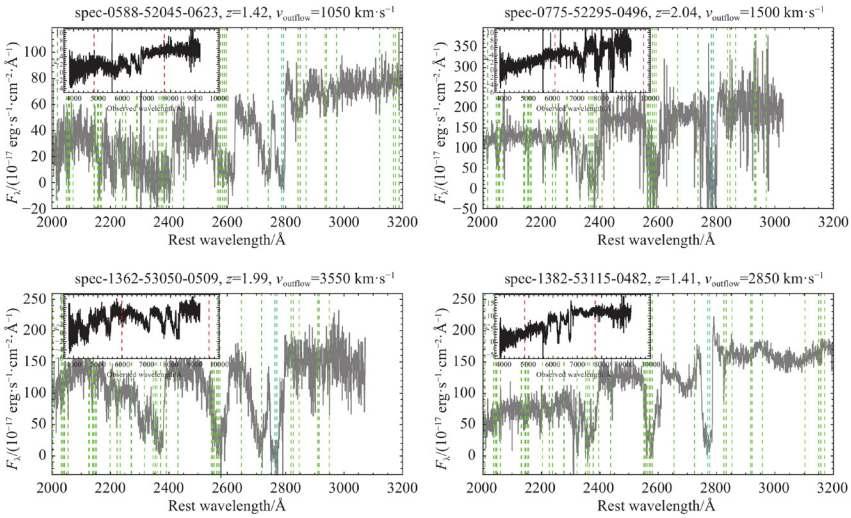

Fig. 3 Example spectra of 4 newly identified FeLoBALQs in this research. Subplots show the spectra in local frame, showing the local frame flux F_λ over local observed wavelength. Red dashed lines represent 2000 Å and 3200 Å in rest frame, the wavelength range limits we decided for FeLoBALQ identification. With transferred into rest frame using redshift z of these FeLoBALQs, the main plots show the spectra in rest frame which are used in the CNN program, showing the calculated rest frame flux F_λ over rest observed wavelength, in decided wavelength range for detail. Green and cyan dashed lines represent absorption lines given in Table 1 in Hall et al.[24], but all blueshifted respected to the original wavelength, with the blueshift velocities i.e. the outflow velocites $\nu_{\rm outflow}$ given in the titles. These absorption lines cannot explain all the absorption features, and the strengths and widths of absorption lines are different among the FeLoBALQ spectra, resulting in different absorption profiles. Regular methods are hard to identify these features, therefore it's necessary to adopt machine learning methods into FeLoBALQ identification.

Using the target sample (SDSS DR7Q quasars with $0.8 < z < 2.125$) and the training sample (containing only the FeLoBALQs identified in previous research, while excluding those identified during the trial run) as a reference, we plotted a color-color diagram for the 160 newly identified FeLoBALQ candidates, as shown in Fig. 4. Since all three samples—the target sample, the training sample, and the new candidate sample—are located outside the Galactic plane, experience minimized Galactic extinction and share the same, narrow redshift range, we performed our statistical analysis using colors derived directly from observed magnitudes. Compared to the target sample, we found that FeLoBALQs are generally redder, with the color differences being more obvious at bluer wavelengths and nearly disappearing in the mid-infrared W1–W2 bands. The physical explanation for this is that the continuum emission contributes more significantly at bluer wavelengths in all quasars. However, in FeLoBALQs, the gaseous outflows cause more pronounced extinction of this continuum than in normal quasars, thereby resulting in their redder colors. The results presented in

Fig. 4 support the theoretical explanation provided above. While sharing a similar distribution with the newly identified FeLoBALQs, previously identified FeLoBALQs are slightly redder on average. This difference can be explained by the following theory: FeLoBALQs with stronger outflow absorption exhibit redder colors. Those FeLoBALQs with stronger absorption consequently display more prominent absorption complexes and troughs in their spectra, which led to their preferential identification in earlier research and resulted in their redder colors on average. Conversely, weaker-absorption FeLoBALQs are generally identified later and thus constitute a larger proportion of the newly identified candidates in this research.

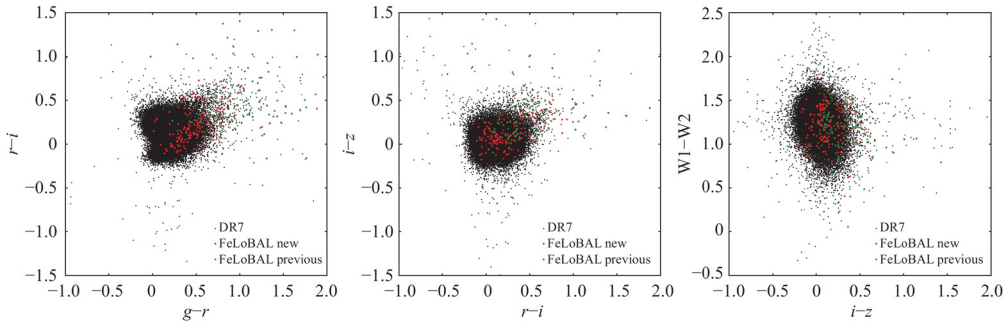

Fig. 4 Color-color diagram for FeLoBALQs and SDSS DR7Q in $0.8 < z < 2.125$ for statistical researching, using 4 colors calculated with SDSS g, r, i, z band magnitude g, r, i, z and WISE W1, W2 band magnitude W1, W2. Red dots represent FeLoBALQs newly identified in this research, green dots represent FeLoBALQs identified in previous research, and black dots represent quasars in DR7Q. FeLoBALQs can be found redder than other quasars, and previously identified FeLoBALQs lightly redder than newly identified ones; these phenomena can be found more obvious on bluer end than on redder end, and the color differences nearly disappear in mid-infrared W1–W2.

The training sample contains 61 FeLoBALQ spectra from SDSS DR7Q. When restricted to the redshift range of $0.8 < z < 2.125$, a total of 221 FeLoBALQ spectra have been identified in SDSS DR7Q to date, which accounts for 0.43% of the total 50931 spectra and represents a proportion slightly higher than the 0.33% reported by Trump et al.[26] in 2006. We posit that this value may still be underestimated, and the actual proportion of FeLoBALQs among the overall quasars is likely greater. One key reason is that FeLoBALQs are intrinsically redder than normal quasars. Furthermore, extinction caused by absorption from gaseous outflows renders them fainter in the observed-frame optical and near-infrared bands, making them easier to confuse with brown dwarfs and leading to their omission during optical source selection. A second reason is that the intense absorption features in FeLoBALQ spectra complicate their population classification and redshift determination. For instance, some FeLoBALQs in our training sample were originally classified as galaxies by SDSS. This misidentification more likely leads to their exclusion during target sample selection.

4. SUMMARY AND PROSPECTS

In this research, using the currently identified FeLoBALQ spectra as the training sample, we first developed a CNN model for FeLoBALQ identification and classification. Subsequently, based on the absorption features of FeLoBALQs, we defined the target quasar redshift range in this research as $0.8 < z < 2.125$. This allowed us to classify all 50931 SDSS DR7Q quasar spectra within this range, which yielded 160 newly identified FeLoBALQ candidates and established a FeLoBALQ fraction of 0.43% for this redshift interval. Finally, we concluded with a brief analysis of the reasons for the redder colors of FeLoBALQs compared to normal quasars, along with the origins of potential statistical biases in research.

Future work will focus on continually refining the CNN program and its structure, improving the training sample, and extending the identification of FeLoBALQs to a sample of 330386 SDSS DR16Q spectra (excluding the 279455 SDSS DR7Q spectra) within the same redshift range. Based on the 0.43% fraction, we expect to identify approximately 1400 FeLoBALQ spectra in the sample, with approximately 1100 of them being newly confirmed, thereby enriching the existing FeLoBALQ catalog and providing substantial data support for related research.

Furthermore, we plan to conduct a series of follow-up observations for the FeLoBALQs in the sample, including high-resolution imaging, spectroscopy, and multi-band photometry. By observing high-resolution images to identify signs of major mergers in the host galaxies of FeLoBALQs, we will resolve the question of whether FeLoBALQs are primarily triggered by such major mergers. High-resolution spectroscopy coupled with multi-band photometry will enable more robust confirmation of the candidates and facilitate determination of key parameters, including black hole mass, bolometric luminosity, outflow velocity and strength, as well as host galaxy star formation rate. Analysis of these derived physical properties will contribute to resolving key questions, such as whether FeLoBALQs are associated with ULIRGs and whether FeLoBALQs signify an evolutionary stage between ULIRGs and quasars. Moreover, by comparing the physical properties of FeLoBALQs across different redshifts, we will investigate whether the incidence rate of FeLoBALQs is correlated with redshift (and thus cosmic age). This investigation holds significant implications for understanding the co-evolution of galaxies and their central black holes.

ACKNOWLEDGEMENTS We acknowledge the SDSS and WISE projects for their high-quality data, the ADS/arXiv/CDS databases for literature mining and sample curation, the topcat and asera software for catalog manipulation and spectral visualization, and the NumPy, SciPy, PyTorch, Astropy, and Specutils packages for data analysis. We extend our sincere gratitude to all these projects, databases, and software tools. We thank the reviewers for their valuable comments and suggestions on this manuscript. We are also indebted to Li Ruancun for his invaluable counsel.

References

1 Di Matteo T., Springel V., Hernquist L., Nature, 2005, 433, 604

2 Debuhr J., Quataert E., Ma C. P., MNRAS, 2011, 412, 1341

3 Moe M., Arav N., Bautista M. A., et al., ApJ, 2009, 706, 525

4 Faucher-Giguère C. A., Quataert E., Murray N., MNRAS, 2012, 420, 1347

5 Yuan M. J., Wills B. J., ApJ, 2003, 593, L11

6 Runnoe J. C., Ganguly R., Brotherton M. S., et al., MNRAS, 2013, 433, 1778

7 Schulze A., Schramm M., Zuo W., et al., ApJ, 2017, 848, 104

8 Rankine A. L., Hewett P. C., Banerji M., et al., MNRAS, 2020, 492, 4553

9 Farrah D., Urrutia T., Lacy M., et al., ApJ, 2010, 717, 868

10 Farrah D., Surace J. A., Veilleux S., et al., ApJ, 2005, 626, 70

11 Farrah D., Lacy M., Priddey R., et al., ApJ, 2007, 662, L59

12 Lawther D., Vestergaard M., Fan X., MNRAS, 2018, 475, 3213

13 Violino G., Coppin K. E. K., Stevens J. A., et al., MNRAS, 2016, 457, 1371

14 Villforth C., Herbst H., Hamann F., et al., MNRAS, 2019, 483, 2441

15 Choi H., Leighly K. M., Terndrup D. M., et al., ApJ, 2022, 937, 74

16 Leighly K. M., Choi H., DeFrancesco C., et al., ApJ, 2022, 935, 92

17 Choi H., Leighly K. M., Dabbieri C., et al., ApJ, 2022, 936, 110

18 Leighly K. M., Choi H., Eracleous M., et al., ApJ, 2024, 966, 87

19 LeCun Y., Bottou L., Bengio Y., et al., Proceedings of the IEEE, 1998, 86, 2278

20 Schneider D. P., Richards G. T., Hall P. B., et al., AJ, 2010, 139, 2360

21 Lyke B. W., Higley A. N., McLane J. N., et al., ApJS, 2020, 250, 8

22 Becker R. H., White R. L., Gregg M. D., et al., ApJ, 2000, 538, 72

23 White R. L., Becker R. H., Gregg M. D., et al., ApJS, 2000, 126, 133

24 Hall P. B., Anderson S. F., Strauss M. A., et al., ApJS, 2002, 141, 267

25 Reichard T. A., Richards G. T., Schneider D. P., et al., AJ, 2003, 125, 1711

26 Trump J. R., Hall P. B., Reichard T. A., et al., ApJS, 2006, 165, 1

27 Urrutia T., Becker R. H., White R. L., et al., ApJ, 2009, 698, 1095

28 Meusinger H., Schalldach P., Scholz R., et al., A&A, 2012, 541, A77

29 Bruni G., González-Serrano J. I., Pedani M., et al., A&A, 2014, 569, A87

30 Zhang S., Zhou H., Wang T., et al., ApJ, 2015, 803, 58

31 Dunn J. P., Wasik B., Holtzclaw C. L., et al., ApJ, 2015, 808, 94

32 McGraw S. M., Shields J. C., Hamann F. W., et al., MNRAS, 2015, 453, 1379

33 Krogager J., Fynbo J. P. U., Heintz K. E., et al., ApJ, 2016, 832, 49

34 Reis I., Poznanski D., Hall P. B., MNRAS, 2018, 480, 3889

35 Schindler J. T., Fan X., Huang Y. H., et al., ApJS, 2019, 243, 5

36 Hahnloser R. H. R., Sarpeshkar R., Mahowald M. A., et al., Nature, 2000, 405, 947

37 Glorot X., Bordes A., Bengio Y., JMLR, 2011, 15, 315

APPENDIX

A FELOBALQS NEWLY IDENTIFIED

Table 1: FeLoBALQs newly identified

SDSS Name	RA/°	Dec/°	SDSS Plate	SDSS MJD	SDSS Fiber	z	SDSS u	SDSS g	SDSS r	SDSS i	SDSS z	WISE W1	WISE W2
J1050-0105	162.5987	−1.0988	276	51909	292	1.54	20.29	19.83	19.32	19.21	19.34	16.06	15.06
J1055+0020	163.8653	0.3338	276	51909	557	1.15	19.75	19.40	18.91	18.78	18.78	15.15	14.17
J1240+0017	190.1199	0.2850	290	51941	635	1.14	19.17	18.84	18.44	18.41	18.47	14.96	13.62
J1310+0104	197.5286	1.0743	294	51986	609	1.31	18.42	17.94	17.66	17.62	17.61	14.25	12.81
J1316-0036	199.1553	−0.6100	295	51985	080	0.93	19.16	18.40	18.08	18.05	17.86	14.34	13.22
J1339+0009	204.9391	0.1628	298	51955	639	1.88	19.23	19.20	19.18	18.91	18.83	15.81	14.62
J1447-0034	221.8142	−0.5677	308	51662	170	1.24	19.68	19.20	18.60	18.51	18.48	14.61	13.38
J1209+0045	182.3844	0.7655	323	51615	370	1.45	18.42	17.63	17.12	17.00	17.04	13.83	12.55
J2336-0107	354.1490	−1.1260	384	51821	011	1.30	19.89	19.66	19.35	19.42	19.36	15.65	14.61
J0338+0056	54.5452	0.9382	415	51810	617	1.63	20.61	19.53	18.61	18.36	18.47	15.83	14.32
J0156+1352	29.1501	13.8701	427	51900	354	1.13	20.21	19.90	19.22	18.99	18.89	14.16	12.62
J0207+1429	31.7576	14.4997	427	51900	602	1.02	20.41	19.85	19.52	19.43	19.39	16.12	15.05
J0805+4535	121.3853	45.5966	439	51877	321	1.56	19.52	18.98	18.57	18.34	18.30	15.08	13.93
J0242-0722	40.7278	−7.3682	456	51910	378	1.22	19.78	19.42	18.90	18.71	18.69	14.38	13.12
J0918+5833	139.7270	58.5610	484	51907	598	1.32	20.38	19.97	19.54	19.19	18.95	15.44	14.41
J0948+6214	147.1910	62.2408	486	51910	607	1.54	21.55	20.56	20.11	19.54	19.49	15.77	14.55
J1239+0235	189.8984	2.5841	521	52326	235	1.31	20.03	19.55	18.95	18.91	18.73	15.60	14.79
J1010+5723	152.5962	57.3918	558	52317	032	1.89	21.09	20.29	19.40	18.85	18.32	15.19	13.95
J1020+0330	155.0584	3.5038	574	52355	017	1.73	18.77	18.61	18.57	18.28	18.27	15.14	13.70
J1056+0549	164.0344	5.8201	580	52368	322	1.33	20.39	20.11	19.73	19.58	19.51	15.75	14.34
J1457+0426	224.3734	4.4488	588	52045	623	1.42	23.27	21.39	20.58	18.98	18.65	14.66	13.31
J1420+6047	215.0429	60.7896	606	52365	110	1.35	22.26	20.68	19.85	19.21	19.05	15.27	14.01
J1628+4755	247.0228	47.9297	625	52145	127	1.52	19.79	19.63	19.26	19.07	19.23	15.73	14.32
J1649+4014	252.4245	40.2489	630	52050	482	1.27	20.04	18.94	18.18	17.85	17.99	14.64	13.24
J2347-1037	356.7977	−10.6285	648	52559	098	1.82	18.85	18.01	17.35	17.04	16.91	13.88	12.41
J2357-0903	359.3263	−9.0540	650	52143	321	1.18	19.89	19.63	19.33	19.25	19.21	15.74	14.41
J0102-0853	15.7069	−8.8957	658	52146	562	1.68	18.82	18.49	18.10	17.76	17.62	14.52	13.52
J0121-0929	20.3634	−9.4847	660	52177	635	1.47	20.77	20.52	19.99	19.26	18.89	16.08	15.45
J2137+1041	324.3145	10.6864	731	52460	076	1.58	22.19	21.12	20.02	19.15	19.02	15.56	14.07
J2204+1327	331.0915	13.4561	735	52519	321	1.70	19.06	18.85	18.66	18.29	18.36	14.87	13.53
J0026+1355	6.5991	13.9232	753	52233	002	1.32	20.21	19.26	18.74	18.65	18.64	15.09	13.65

Tabel 1 Continued

SDSS Name	RA/°	Dec/°	SDSS Plate	SDSS MJD	SDSS Fiber	z	SDSS u	SDSS g	SDSS r	SDSS i	SDSS z	WISE W1	WISE W2
J1120+6204	170.0069	62.0832	775	52295	496	2.04	25.00	20.98	19.46	19.02	18.36	14.92	13.89
J1202+6317	180.5080	63.2998	778	52337	362	1.48	20.14	19.86	19.34	19.09	18.97	16.05	14.98
J1448+5639	222.1614	56.6553	791	52435	103	1.67	21.84	20.65	20.39	19.66	19.18	15.94	15.02
J1534+5147	233.6083	51.7924	795	52378	140	1.77	19.64	19.45	18.99	18.46	18.34	14.77	13.74
J1530+5115	232.6190	51.2540	795	52378	279	1.94	19.46	19.26	19.21	18.92	18.87	15.41	14.15
J1233+0608	188.3692	6.1423	845	52381	530	1.19	18.83	18.42	18.16	18.20	18.13	14.42	13.00
J1319+0550	199.9602	5.8458	851	52376	524	1.06	20.36	19.93	19.28	18.99	18.89	15.68	14.76
J1337+0527	204.4713	5.4629	853	52374	531	1.74	19.55	19.21	18.68	18.14	17.83	15.15	14.07
J1344-0158	206.2090	−1.9786	913	52433	381	0.96	19.85	19.31	19.02	19.00	18.75	14.69	13.59
J1348-0153	207.1283	−1.8994	914	52721	353	0.82	20.19	19.58	19.15	19.08	18.94	15.03	13.81
J1527-0210	231.8533	−2.1820	924	52409	003	1.17	20.13	20.04	19.54	19.47	19.49	15.68	14.35
J0743+2209	115.8371	22.1625	927	52577	003	2.06	20.13	19.81	19.43	18.75	18.14	15.60	14.73
J1010+4518	152.7249	45.3047	943	52376	507	1.78	19.65	18.43	17.63	17.21	16.92	13.36	12.24
J1011+5712	152.8634	57.2049	946	52407	321	1.15	18.07	18.08	17.93	17.98	18.16	14.94	13.57
J1006+0513	151.5236	5.2303	996	52641	243	0.97	20.15	19.51	18.89	18.67	18.30	13.31	12.03
J0801+3153	120.4164	31.8916	1061	52641	479	1.66	19.24	18.87	18.45	18.24	18.33	15.87	15.00
J2140-0653	325.0573	−6.8969	1177	52824	406	1.72	21.90	20.37	19.82	19.29	18.93	15.00	13.47
J0834+0613	128.6812	6.2261	1187	52708	341	1.44	19.78	19.34	19.03	18.87	18.85	16.03	14.76
J1145+1100	176.4844	11.0051	1226	52734	375	0.94	19.95	19.34	18.98	18.81	18.56	15.21	14.31
J1041+0925	160.4975	9.4231	1240	52734	589	1.23	20.31	19.97	19.30	19.17	19.06	15.62	14.73
J0811+2452	122.7508	24.8753	1265	52705	540	1.07	20.75	20.12	19.84	19.76	19.63	15.89	14.85
J0912+3515	138.1266	35.2607	1273	52993	371	1.05	19.48	18.96	18.82	18.93	18.89	15.91	14.79
J1302+4859	195.7349	48.9979	1281	52753	306	0.87	18.77	18.30	18.07	18.09	17.94	14.16	12.95
J1333+4916	203.4295	49.2731	1283	52762	411	1.39	19.89	19.76	19.00	18.98	18.89	15.59	14.57
J0912+0915	138.2305	9.2574	1301	52976	325	1.35	19.60	19.42	19.00	18.89	18.86	15.24	13.89
J1239+5755	189.8757	57.9288	1316	52790	623	0.97	19.19	18.51	18.07	17.97	17.82	14.51	13.54
J1359+5532	209.7715	55.5383	1324	53088	331	1.21	19.04	18.41	18.14	18.31	18.39	15.64	14.46
J1054+4428	163.5484	44.4790	1362	53050	509	1.99	22.11	20.54	19.38	19.59	18.56	15.20	13.89
J1440+3710	220.0093	37.1829	1382	53115	482	1.41	23.18	20.30	18.99	18.06	17.78	13.94	12.70
J1155+4659	178.7997	46.9844	1446	53080	161	1.30	19.73	19.21	18.74	18.62	18.62	14.68	13.25
J0003+0010	0.7639	0.1721	1489	52991	597	1.52	21.33	20.91	20.72	20.48	20.48	17.11	15.35
J1646+1943	251.7298	19.7169	1569	53168	135	1.95	20.96	20.14	19.65	19.12	19.33	15.83	14.86
J1612+2516	243.1798	25.2691	1575	53493	311	1.81	19.16	19.40	19.18	18.73	18.59	15.62	14.79
J1617+2509	244.4265	25.1595	1576	53496	249	1.79	19.44	18.95	18.12	17.68	17.78	14.87	14.01
J1539+3205	234.9968	32.0863	1581	53149	197	1.51	20.07	19.80	19.51	19.09	18.71	15.68	14.30

Tabel 1 Continued

SDSS Name	RA/°	Dec/°	SDSS Plate	SDSS MJD	SDSS Fiber	z	SDSS u	SDSS g	SDSS r	SDSS i	SDSS z	WISE W1	WISE W2
J1547+3230	236.9257	32.5133	1581	53149	637	1.31	20.30	20.44	20.08	20.11	19.99	15.73	14.69
J0823+2446	125.9606	24.7814	1585	52962	639	1.77	20.71	20.19	19.45	18.79	18.54	14.65	13.24
J1539+0737	234.9619	7.6300	1724	53859	252	1.10	20.97	19.68	19.09	19.14	19.10	15.14	13.76
J1610+0713	242.5280	7.2215	1729	53858	637	1.35	19.72	19.34	19.04	18.98	18.88	15.17	13.77
J0743+4357	115.9192	43.9516	1736	53052	148	1.86	21.19	20.17	18.94	18.18	17.63	13.44	12.27
J0949+1237	147.4285	12.6292	1743	53054	355	1.67	19.73	19.29	18.72	18.43	18.49	15.44	14.24
J1022+1301	155.7053	13.0236	1746	53062	151	1.22	22.17	20.80	19.55	19.13	18.77	14.23	12.62
J1043+1327	160.8329	13.4635	1749	53357	280	1.46	20.65	19.48	18.51	18.06	17.80	14.08	12.98
J1102+1438	165.5593	14.6479	1751	53377	350	1.37	19.57	18.99	18.48	18.37	18.28	14.45	13.12
J0832+0758	128.1919	7.9703	1758	53084	035	1.90	19.89	19.55	19.08	18.50	18.17	15.41	15.01
J0825+0652	126.2604	6.8801	1758	53084	284	1.45	20.79	20.42	19.86	19.54	19.29	14.88	13.12
J1222+1423	185.6569	14.3975	1766	53468	030	1.01	19.59	19.27	18.90	18.84	18.61	15.08	13.69
J1336+0830	204.1352	8.5167	1801	54156	530	0.81	19.31	18.74	18.34	18.23	18.13	14.44	13.36
J1335+1018	203.8563	10.3108	1802	53885	410	1.11	–	–	–	–	–	–	–
J1432+0547	218.0984	5.7919	1827	53531	064	0.99	19.63	19.09	18.89	18.88	18.68	15.53	14.32
J1507+2906	226.7806	29.1020	1845	54144	311	1.07	18.83	18.19	17.99	18.01	17.87	14.90	13.81
J1543+2640	235.7635	26.6812	1849	53846	577	1.92	21.44	19.86	18.61	18.41	17.91	15.16	14.13
J1553+2358	238.4001	23.9767	1850	53786	102	0.92	19.67	19.32	18.51	18.30	18.02	14.93	14.02
J1548+2432	237.1518	24.5477	1850	53786	319	1.38	19.84	19.60	19.30	19.18	19.14	15.56	14.16
J1551+2544	237.7571	25.7400	1850	53786	544	1.35	20.04	19.95	19.26	19.21	19.06	15.35	14.23
J0800+1943	120.0628	19.7332	1922	53315	474	1.25	20.64	19.69	18.75	18.44	18.39	14.77	13.34
J1022+3459	155.5697	34.9916	1957	53415	221	1.94	21.51	20.39	19.38	18.73	18.36	15.11	14.15
J1029+3701	157.4323	37.0242	1957	53415	601	1.34	20.44	20.47	20.05	19.79	19.82	16.05	14.79
J1326+2839	201.5101	28.6660	1978	53473	318	1.73	20.68	19.98	19.77	19.12	18.74	15.20	14.04
J1232+4106	188.0754	41.1105	1984	53433	363	1.33	20.25	19.60	19.08	18.86	18.83	15.80	14.57
J1234+3839	188.6472	38.6542	1992	53466	585	1.85	19.09	18.83	18.47	17.93	17.62	14.83	13.94
J1147+3734	176.9181	37.5775	1997	53442	143	1.30	21.70	20.26	19.32	18.99	18.78	14.18	12.72
J1306+3258	196.6789	32.9676	2006	53476	018	1.43	19.74	19.60	19.12	19.01	18.92	15.63	14.54
J1245+3412	191.3790	34.2026	2020	53431	639	1.25	19.59	19.37	18.95	18.77	18.70	14.98	13.48
J0206+2227	31.5946	22.4512	2046	53327	433	1.70	18.13	17.50	16.99	16.77	16.84	14.04	13.04
J0133+2333	23.4287	23.5521	2064	53341	318	0.91	19.51	18.84	18.53	18.55	18.31	14.54	13.29
J1409+2729	212.2780	27.4947	2120	53852	620	1.93	22.76	21.95	20.06	19.03	18.58	14.77	13.40
J1635+1415	248.8957	14.2657	2204	53877	441	1.44	19.00	18.31	17.83	17.61	17.57	13.80	12.22
J1215+2934	183.9463	29.5694	2232	53827	314	1.53	19.75	19.06	18.46	17.93	17.67	14.35	13.16
J1230+2759	187.7432	27.9901	2235	53847	463	0.95	21.76	21.53	19.65	19.24	18.85	15.05	13.71

Tabel 1 Continued

SDSS Name	RA/°	Dec/°	SDSS Plate	SDSS MJD	SDSS Fiber	z	SDSS u	SDSS g	SDSS r	SDSS i	SDSS z	WISE W1	WISE W2
J1248+2846	192.1400	28.7691	2239	53726	205	1.60	20.58	19.69	18.89	18.51	18.18	14.29	13.09
J0813+1345	123.3874	13.7543	2270	53714	272	1.62	20.80	19.29	18.53	18.12	17.95	14.58	13.44
J0033+0632	8.3985	6.5354	2327	53710	256	1.50	19.95	19.25	18.69	18.32	18.27	14.23	12.78
J1017+2303	154.3460	23.0562	2346	53734	090	1.72	–	–	–	–	–	–	–
J1000+2006	150.2145	20.1102	2363	53763	029	1.49	20.89	20.19	19.60	19.10	19.03	15.59	14.20
J1022+2158	155.6002	21.9758	2365	53739	625	1.17	18.86	18.61	18.27	18.14	18.09	14.32	12.97
J0249+3320	42.4427	33.3497	2378	53759	281	1.29	19.70	18.75	18.09	17.87	17.75	14.27	12.82
J1042-0008	160.6780	−0.1392	2409	54210	285	1.45	20.81	19.68	19.10	18.74	18.64	15.00	13.38
J1045+2210	161.2578	22.1779	2477	54058	054	1.15	18.36	17.80	17.37	17.23	17.16	13.25	11.79
J1050+2004	162.6271	20.0728	2482	54175	372	1.65	21.00	19.62	18.76	18.23	17.87	15.19	15.13
J1114+2222	168.5054	22.3699	2492	54178	536	2.12	19.42	18.76	18.37	18.20	17.76	14.75	13.73
J1133+2231	173.2800	22.5186	2500	54178	573	1.39	19.83	19.38	19.01	18.66	18.55	15.02	13.80
J1632+0942	248.0821	9.7132	2532	54589	635	1.31	19.84	18.93	18.53	18.34	18.30	14.81	13.35
J0849+1125	132.3015	11.4273	2574	54084	371	1.33	20.68	20.19	19.47	19.08	18.84	14.24	12.80
J1209+1651	182.2910	16.8590	2595	54207	025	1.04	19.32	19.09	18.87	18.88	18.70	14.98	13.67
J1214+1749	183.6254	17.8187	2596	54207	501	1.05	19.85	19.26	18.97	18.98	18.86	15.16	13.94
J1227+1750	186.9019	17.8497	2598	54232	463	1.17	18.18	17.59	17.23	17.21	17.26	13.72	12.56
J1259+2057	194.7994	20.9606	2616	54499	373	1.25	19.19	19.13	19.04	19.04	19.14	15.38	14.27
J1305+1932	196.4866	19.5444	2616	54499	627	1.50	20.38	20.03	19.60	19.20	19.06	15.82	14.33
J1334+2004	203.5659	20.0771	2641	54230	536	1.07	21.10	20.03	19.35	19.16	18.83	14.79	13.74
J1247+2323	191.9088	23.3933	2648	54485	612	1.51	19.96	19.70	19.20	18.92	18.83	15.51	14.48
J1316+2507	199.0522	25.1236	2663	54234	581	0.98	22.23	20.72	20.21	20.05	20.00	17.62	18.35
J1338+2246	204.6095	22.7751	2666	54230	299	1.18	18.74	18.44	18.20	18.09	17.98	13.85	12.35
J1439+1535	219.9281	15.5876	2748	54234	527	1.72	21.59	20.23	19.34	18.47	18.18	14.63	13.16
J1524+1153	231.0966	11.8867	2753	54234	055	1.42	20.87	19.78	18.99	18.47	18.42	15.12	13.67
J1417+1743	214.2783	17.7187	2759	54534	382	1.28	20.46	19.40	18.58	18.19	17.89	13.50	12.13
J1533+1500	233.4245	15.0165	2768	54265	450	1.43	23.53	22.76	20.56	19.50	19.24	15.43	14.13
J1500+1648	225.0874	16.8152	2778	54539	012	1.12	19.17	18.52	18.01	18.01	17.97	14.40	12.99
J1533+5650	233.3126	56.8458	2883	54525	637	1.22	20.50	20.35	19.97	20.02	20.05	15.92	14.81
J1059+0934	164.8402	9.5696	2886	54498	639	1.20	19.70	19.42	19.26	19.33	19.25	15.90	14.99
J0753+0822	118.3232	8.3757	2945	54505	243	1.39	19.48	18.61	18.31	18.08	18.19	15.41	14.17
J0925+3251	141.4070	32.8502	2961	54550	035	1.37	20.97	20.99	20.71	20.78	20.90	16.61	15.65
J0921+3243	140.4516	32.7330	2961	54550	102	1.39	20.85	20.71	20.52	20.40	20.37	16.77	15.80
J0914+3253	138.6990	32.8908	2961	54550	400	1.36	21.53	20.95	20.41	20.15	20.10	15.85	14.62
J1035-0029	158.9373	−0.4902	273	51957	069	2.08	20.27	19.62	19.07	18.80	18.53	15.03	13.66

Tabel 1 Continued

SDSS Name	RA/°	Dec/°	SDSS Plate	SDSS MJD	SDSS Fiber	z	SDSS u	SDSS g	SDSS r	SDSS i	SDSS z	WISE W1	WISE W2
J1053-0058	163.4703	−0.9813	276	51909	139	1.57	19.02	18.41	17.95	17.57	17.48	14.27	12.96
J1056+0012	164.0902	0.2121	276	51909	551	1.71	21.58	20.86	20.50	19.99	19.87	15.66	14.23
J1104-0004	166.1701	−0.0782	277	51908	077	1.35	19.98	19.32	18.99	18.94	18.88	15.41	14.12
J1107-0051	166.8686	−0.8563	278	51900	214	1.73	21.36	20.68	19.63	19.03	18.70	14.42	13.01
J1133-0057	173.4220	−0.9611	282	51658	215	1.70	21.09	20.18	19.39	18.67	18.30	14.24	12.79
J1158-0043	179.7203	−0.7172	285	51930	189	0.98	21.63	20.50	19.70	19.38	18.83	14.53	13.55
J1607+0058	241.9956	0.9763	345	51690	363	1.79	20.79	19.95	19.64	19.10	18.85	15.40	14.18
J1716+6434	259.0158	64.5730	350	51691	145	1.53	18.31	17.78	17.31	17.18	17.24	14.72	13.74
J1723+6547	260.8089	65.7962	350	51691	604	1.44	17.63	17.35	16.94	16.87	16.87	14.02	12.93
J1733+5520	263.3785	55.3419	358	51818	127	1.20	19.88	19.21	18.71	18.46	18.15	14.52	13.31
J1729+5547	262.2890	55.7857	358	51818	284	1.43	19.24	19.24	18.69	18.51	18.38	15.44	14.39
J1725+5254	261.2527	52.9139	359	51821	139	1.36	19.52	19.42	19.15	19.24	19.04	15.70	14.37
J1736+5855	264.2424	58.9172	366	52017	638	1.62	21.86	20.92	20.03	19.55	19.24	15.62	14.44
J2339-0029	354.8934	−0.4924	385	51877	221	2.03	21.78	20.81	20.19	19.85	19.28	15.71	14.43
J0321-0013	50.4635	−0.2230	413	51929	102	1.15	20.30	20.09	19.61	19.67	19.78	15.65	14.57
J0925+0136	141.2972	1.6053	475	51965	310	1.80	18.38	18.31	17.95	17.54	17.47	14.14	13.08
J1235+0132	188.9581	1.5480	520	52288	001	1.29	21.40	20.81	19.94	19.16	18.87	14.96	13.99
J0857+5031	134.4673	50.5234	551	51993	538	1.39	20.40	20.06	19.47	19.16	18.92	14.84	13.37
J1040+6122	160.2032	61.3792	561	52295	329	1.16	19.77	19.05	18.48	18.29	18.12	14.12	12.86
J0849+0217	132.4738	2.2860	564	52224	010	1.11	19.55	19.17	18.83	18.77	18.69	14.86	13.69
J1045+0540	161.3088	5.6755	578	52339	574	0.99	20.60	19.95	19.38	19.24	18.96	15.16	14.11
J1432+0352	218.2217	3.8823	585	52027	159	1.69	20.72	19.98	19.61	19.09	18.80	15.03	13.59
J1355+6152	208.7761	61.8694	605	52353	319	1.36	18.93	18.72	18.31	18.14	18.12	14.69	13.44
J1507+5804	226.9116	58.0703	610	52056	064	1.45	19.61	19.04	18.30	18.19	18.11	14.97	13.90